

An extended transfer operator approach for time-consistent coherent set analysis

Benedict Lünsmann,¹ Rahel Vortmeyer-Kley,² and Holger Kantz¹

¹*Max Planck Institute for the Physics of Complex Systems (MPIPKS), 01187 Dresden, Germany*

²*Leibniz Institute for Baltic Sea Research (IOW), 18119 Rostock-Warnemünde, Germany*

Coherent oceanic mesoscale structures, especially the non-filamenting cores of oceanic eddies, have gained a lot of attention in recent years. These Lagrangian structures are considered to play a significant role in oceanic transport processes which, in turn, impact marine life, weather and potentially even the climate itself. Answering questions regarding these phenomena requires robust tools for the detection and identification of these structures. In this article, we use transfer operator ideas to develop a novel method for the identification of weakly-mixing coherent volumes in oceanic velocity field data sets. Unlike other methods, the approach focuses on maximizing consistency over longer time periods. We employ a time-centralized transfer operator approach with practical modifications to identify potential structures in predetermined domains and couple adjacent time steps to decide how to conduct the final partitioning. The analysis pipeline includes plausibility checks that give further insights into the stability and coherence of the inferred structure. The presented method is able to find changing masses of maximal coherence in stationary and non-stationary toy models and yields good results when applied to field data.

The following article has been submitted to Chaos: An Interdisciplinary Journal of Nonlinear Science. After it is published, it will be found at [Link](#).

Eddies, non-filamenting coherent oceanic mesoscale structures, are considered to impact oceanic transport processes and marine life in many ways. Studying their impact necessitates the development of robust methods of identification. Here, we present and test an extended and modified two-step transfer operator approach that facilitates the extraction of time-consistent coherent sets.

I. INTRODUCTION

Horizontal transport processes in the upper layer of the ocean are dominated by hydrodynamic mesoscale structures like jets, fronts and eddies. Their emergence, disappearance and complicated interplay orchestrates an ever-changing chaotic flow that stirs and mixes the involved fluid volume. However, not all parts of the ocean surface mix equally fast. Coherent volumes resist filamentation for finite-time. They coherently transport trapped water masses in ambient water of different properties and thus contribute to the patchiness of scalar fields like temperature and salinity^{1–5}. This in return implies impacts on marine life^{2,5–9} and possibly the climate³.

Algae production, in particular, is affected by mesoscale structures in the velocity field in various subtle and obvious ways. These structures are responsible for the generation of variability and filamentation of plankton patches on smaller scales^{2,10} and appear to have a strong impact on large scale plankton distributions pre-

sumably due to the formation of hydrodynamic biological niches⁷.

Eddies constitute one such potential niche. These mesoscale structures trap their rotating fluid volume while being able to generate vertical currents whereby they actively change the biogeochemical conditions for algae growth inside their boundaries^{9,11,12}. In this regard, studies of toy models have shown that the restriction of upwelling to the vicinity of eddy centers may result in overall reduced algae production¹³ and entrainment of nutrients may result in a confined bloom inside an eddy⁶.

In order to study the impact of eddies it is first necessary to develop reliable methods for the boundary estimation of finite-time coherent sets that constitute the eddy core. This is a non-trivial task and especially difficult in turbulent coastal regions.

Two fundamentally different classes of such eddy boundary detection approaches have to be distinguished: traditional Eulerian methods and more recent Lagrangian methods. Eulerian methods operate on velocity field snapshots. Popular examples are the Okubo-Weiss criterion^{14–17} and any SSH-field (sea surface height)^{11,18,19}, streamline²⁰ or vorticity²¹ based approach. Lagrangian methods focus on trajectories of fluid parcels. This class includes FTLE/FSLE (finite time/size Lyapunov exponent)^{22,23} based methods, Lagrangian descriptors^{24,25}, simple clustering approaches^{26,27}, geometric approaches^{28–30} and transfer operator based approaches^{31–34} (for a comparison of methods see³⁵). Since coherent volumes are of Lagrangian nature, only approaches of the latter class are able to provide accurate results. Yet, Eulerian methods are computationally less expensive and have proven to yield good approximations in real velocity fields.

In this paper, we present a novel two-step approach based on transfer operators for the inference of coherent eddy cores. The approach requires a preselected sequence of regions that follows the temporal development

of a potentially coherent structure. First, each region of interest is analyzed independently using a modified time-centralized transfer operator approach to quantify the affiliation of individual region parts to the central eddy core (compare³¹). The modifications account for coastal boundary fluxes as well as domain separation and enforce the inference of circular structures (compare³⁶). In the second step, we use short-time transfer operators to couple adjacent time-steps (compare³⁷). This way, for given partitions, we are able to compute the probability to stay within the boundaries of the estimated coherent core. The partitionings are then optimized to maximize the overall probability to stay within these boundaries. At several points in the analysis pipeline, we check for changes in the coherence to guarantee the plausibility of the returned solution.

Our approach has several advantages over existing alternatives. First, it focuses on temporal consistency and couples the results of individual time steps to generate a reliable result over larger time windows. Most other approaches yield structures which are instantaneous and localized in time. These methods construct results for other points in time simply by integrating the obtained solution. Secondly, it decouples the size of the overall analysis window and the integration time needed to define coherence. Thus, the approach accepts a slight exchange of fluid volume across the inferred boundaries while strongly reducing the generation of filaments. This feature appears to be useful for the study of eddy cores over longer time periods.

We test our approach on stationary velocity fields³⁶ and a commonly used Bickley jet model³⁸ before studying its performance on actual oceanic flows in the Western Baltic Sea. Our results show that the approach is well able to infer coherent sets in stationary and time-dependent toy model cases (see Sec. III A and Sec. III B). As expected, actual oceanic flows prove to be more challenging. The results illustrate how to tackle potential difficulties and point towards additional insights that can be obtained using the proposed approach (see Sec. III C).

The presented approach is successfully applied in³⁹ to facilitate the study of plankton population dynamics in coherent water masses in the Baltic Sea. There, the identification of coherent sets directly follows ideas of this article (see Sec. III C).

II. METHOD

The presented method is a modified time-centralized transfer operator approach with two steps that aims to identify a coherent set contained in a preselected sequence of regions. In the following, we first explain step one, the individual treatment of regions (Sec. II A). Subsequently, we show how adjacent time steps are coupled to optimize the partitioning in step two (Sec. II B). And finally, we introduce ways to check the plausibility of the returned result (Sec. II C).

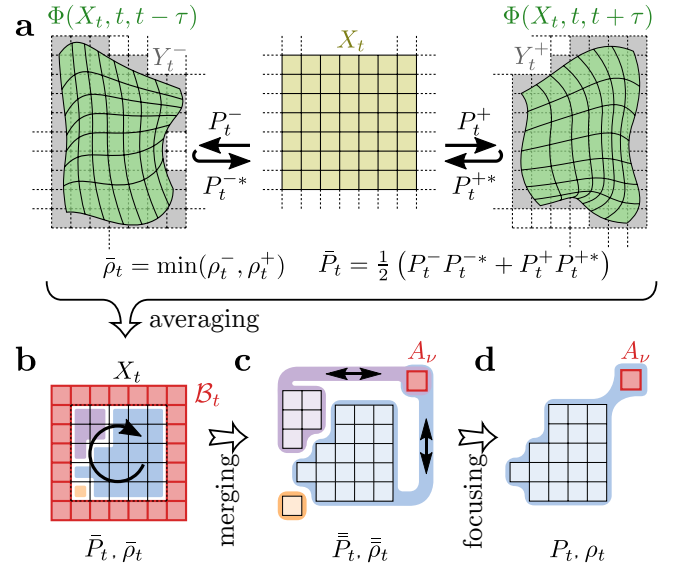


FIG. 1. Construction of the modified time-centralized transfer operator P_t . **a)** For each domain X_t , we compute the transfer operators P_t^+ , P_t^- and their densities ρ_t^+ , ρ_t^- using the flow Φ . Then, we compute the minimal mass vector $\bar{\rho}_t$ to determine the time-reversed operators P_t^{*-} and P_t^{*+} . **b)** The influences of future and past transport on mixing are averaged to create the time-centralized operator \bar{P}_t . We couple all potential filaments by merging the boundary B_t (red) into one virtual tile A_v (also red) and obtain **c)** the transfer operator \bar{P} . This graph of transfer probabilities potentially contains multiple components, some of which are coupled via the virtual tile A_v (purple, blue) and some that might be disconnected (orange). **d)** Focusing on the largest strongly connected component that is connected to the virtual tile A_v (blue) yields P_t .

A. Transfer Operator Approach

The presented approach aims, like most transfer operators, to capture the material transport of a flow Φ by approximating its Frobenius-Perron operator \mathcal{P} , an operator that describes how densities evolve under Φ . Analyzing this operator allows the inference of sets that are almost-invariant under evolution of the flow Φ .

Since derivation of a closed mathematical solution of the Frobenius-Perron operator \mathcal{P} is rarely possible and thus unrealistic for actual oceanic flows, the operator is approximated by a transfer probability matrix that specifies the probability of transitions between different region parts under the flow Φ . This graph of transfer probabilities can then be analyzed to find weakly communicating partitions. Essentially, the search for non-communicating sets becomes a graph cut problem. In addition, the transfer probability matrix allows for modifications to focus on specific structures³⁶ or to facilitate the analysis (see below).

We start with a sequence of regions that track and contain the trajectory of exactly one eddy. In the first step of the analysis, each region is treated individually using a time-centralized transfer operator approach with certain modifications (Sec. II A 1). The modifications include the treatment of coastal boundary fluxes (Sec. II A 2), the

enforcement of circular solutions (Sec. II A 4) and measures to avoid domain separation (Sec. II A 5). The results of this analysis is a sequence of indicator vectors that quantify the affiliation of region parts to the eddy core (Sec. II A 6).

1. Transfer Operator

In order to capture the transport properties of a time-dependent flow $\Phi : \mathcal{X} \times \mathbb{R} \times \mathbb{R} \rightarrow \mathcal{X}$ at time t over an integration time τ , we introduce a domain-covering partitioning of the domain of interest $X_t \subseteq \mathcal{X}$

$$X_t = \bigcup_{i=1}^N A_{t,i} \quad \text{with} \quad A_{t,i} \cap A_{t,j} = \emptyset \quad \forall i \neq j \quad (1)$$

and choose a partitioning that contains its image $Y_t^+ := \Phi(X_t, t, t + \tau)$

$$Y_t^+ \subseteq \bigcup_{i=1}^M B_{t,i}^+ \quad \text{with} \quad B_{t,i}^+ \cap B_{t,j}^+ = \emptyset \quad \forall i \neq j. \quad (2)$$

Furthermore, we define an appropriate mass vector $\rho_t \in \mathcal{R}_+^N$ that characterizes the mass contained in each subset, e.g., $\rho_{t,i} = \mu(A_{t,i})$ with $\mu(\cdot)$ being the Lebesgue measure. Then, we apply Ulam's method⁴⁰ to approximate the Frobenius-Perron operator $\mathcal{P}(t, t + \tau)$ of the flow $\Phi(\cdot, t, t + \tau)$ (see Fig. 1a).

Accordingly, we approximate the transport probability $p(B_{t,j}, t + \tau | A_{t,i}, t)$ from $A_{t,i}$ to $B_{t,j}$ by counting the fractions of tracers that are injected in $A_{t,i}$ at time t and arrive in $B_{t,j}$ at time $t + \tau$:

$$p(B_{t,j}, t + \tau | A_{t,i}, t) \approx P_{t,ij}^+ \quad (3)$$

$$= \frac{\# \text{ tracers that arrived in } B_{t,j}}{\# \text{ tracers released inside } A_{t,i}} \quad (4)$$

Thus, the mass transported from tile $A_{t,i}$ to tile $B_{t,j}$ by the flow $\Phi(\cdot, t, t + \tau)$ is given by $\rho_{t,i} P_{t,ij}^+$.

Analogously, we approximate the Frobenius-Perron operator $\mathcal{P}(t, t - \tau)$ of the flow into the past $\Phi(\cdot, t, t - \tau)$ and obtain another transport probability matrix $P_{t,ij}^-$ (see Fig. 1a).

2. Reduction to Oceanic Transport

In oceanic flows the rules set for the flow across the coastline are crucial for the investigation of coastal material transport.

For reasons of simplicity, we decided to ignore all mass that is washed ashore. Hence, we focus on the water body that is only involved in pure oceanic transport. This is done by deleting all tracers that cross the coastline before computing elements of the transfer probability matrix [Eq (4)] and adjusting the entry of the mass vector ρ_t in proportion of the number of deleted tracers.

However, this way, the mass vector ρ_t depends on the flow. Hence, we generally obtain two different mass vectors ρ_t^+ and ρ_t^- , one for each time-direction.

The mass vector $\bar{\rho}_t$ that disregards all mass involved in coastal boundary fluxes is thus given by

$$\bar{\rho}_{t,i} = \min(\rho_{t,i}^-, \rho_{t,i}^+). \quad (5)$$

We use this mass vector $\bar{\rho}_t$ as a common basis for mass transport into the future and past.

3. Time-centralized transfer operator

We then compute the time-centralized transfer probability matrices \bar{P}_t using the transfer operators in both time directions P_t^\pm and their common mass vector $\bar{\rho}_t$ (see Fig. 1a).

This is done by using detailed balance to obtain the time-reversed operator of P_t^\pm

$$P_{t,ij}^{\pm,*} := \frac{\bar{\rho}_j}{\sum_j \bar{\rho}_j P_{t,ji}^\pm} P_{t,ji}^\pm \quad (6)$$

and by averaging future and past effects

$$\bar{P}_t := \frac{1}{2} (P_t^+ P_t^{+,*} + P_t^- P_t^{-,*}). \quad (7)$$

The operator \bar{P}_t describes the joint effects of transporting mass into the future and past, adding diffusion (generated by coarse-graining) and transporting back into the present³¹.

4. Mixing Boundary

We plan to partition the graph of transfer probabilities described by the time-centralized transfer operator \bar{P}_t in subgraphs with minimal inter-subgraph material transport such that one of the subgraphs can be identified with the central eddy core.

Since, in most cases, the eddy is surrounded by multiple non-communicating filaments, multiple cuts are necessary to uncover the central eddy core. Many transfer operator approaches rely on clustering techniques to determine the necessary number of cuts and subsequently the central structure of the enclosed flow^{41–45}. Instead, we argue, that it is simpler to reduce the number of necessary cuts because the overall geometry of the eddy is known. We know, that tiles at the boundary of the investigated domain are not part of the eddy core but rather part of the filaments surrounding it. By artificially connecting all filaments, we leave just one efficient graph-cut: the boundary separating the inner eddy core from the outer embedding flow. Essentially, this makes horizontal and vertical graph cuts inefficient and enforces the inference of circular structures.

We thus merge all tiles contained in the boundary $A_{t,i} \in \mathcal{B}_t$ into one virtual tile $A_{t,\nu}$ and modify the transfer probability matrix \bar{P}_t accordingly while leaving the structure of material transport inside the boundary intact (see Fig. 1b). For simplicity, let $I = \{1, \dots, N - n\}$ and $J = \{N - n + 1, \dots, N\}$ be the indices of tiles outside and inside the boundary \mathcal{B}_t and let $\nu = N - n + 1$ be

the final index of the virtual tile. Then the new transfer probability matrix $\bar{P}_t \in \mathbb{R}_+^{\nu \times \nu}$ is given by

$$\bar{P}_{t,ij} = \bar{P}_{t,ij}, \quad \bar{P}_{t,\nu j} = \frac{\sum_{i \in J} \bar{\rho}_{t,i} \bar{P}_{t,ij}}{\sum_{i \in J} \bar{\rho}_{t,i}}, \quad (8)$$

$$\bar{P}_{t,i\nu} = \sum_{j \in J} \bar{P}_{t,ij}, \quad \bar{P}_{t,\nu\nu} = \frac{\sum_{i \in J} \bar{\rho}_{t,i} \bar{P}_{t,ij}}{\sum_{i \in J} \bar{\rho}_{t,i}}. \quad (9)$$

The new mass vector is

$$\bar{\rho}_{t,i} = \bar{\rho}_{t,i}, \quad \bar{\rho}_{t,\nu} = \sum_{i \in J} \bar{\rho}_{t,i}. \quad (10)$$

5. Largest Strongly Connected Component

The construction of the time-directed transfer operators P_t^\pm , the restriction to oceanic fluid transport and the merging of the boundary may lead to the separation of the domain in non-communicating regions.

Since we are not interested in the inference of isolated tiles (e.g., regions that are cut-off by the cost-line), we reduce our analysis to the largest strongly connected component that is connected to the boundary. In other words, we drop anything that is isolated and if two or more components are only connected via the virtual tile A_ν we keep the larger one (see Fig. 1c/d).

The transfer probability matrix \bar{P}_t is modified to account for these changes. We refer to the resulting and final transfer operator as P_t and the final mass vector as ρ_t .

6. Indicator Vector

We seek to partition the graph described by the transfer operator P_t into two sets, inner core $C_t \subset X_t$ and outer flow $S_t \subset X_t$, such that the inter-set mass transport \mathcal{M} is minimized. Let $z_t \in \{-1, 1\}^\nu$ be an indicator vector such that $z_{t,i} = 1 \Leftrightarrow A_{t,i} \in C_t$ then this mass transport is given by

$$\mathcal{M} = \frac{1}{4} \sum_{i,j=1}^{\nu} \rho_{t,i} P_{t,ij} (z_{t,i} - z_{t,j})^2 \propto z_t^\top L_t z_t, \quad (11)$$

$$L_{t,ij} = \delta_{ij} \sum_{k=1}^{\nu} \frac{\rho_{t,i} P_{t,ik} + \rho_{t,k} P_{t,ki}}{2} + \frac{\rho_{t,i} P_{t,ij} + \rho_{t,j} P_{t,ji}}{2}. \quad (12)$$

Wherein L_t is a Laplacian matrix and δ_{ij} is the Kronecker-delta. We now search for an indicator vector z_t that minimizes this expression. Unfortunately, without further assumptions this problem is NP-hard.

Relaxing the problem by letting indicator elements take real values $\tilde{z}_t \in \mathbb{R}^\nu$ while establishing conditions to avoid trivial solutions ($\sum_i \tilde{z}_{t,i} \rho_{t,i} = 0$, $\sum_i \tilde{z}_{t,i}^2 \rho_{t,i} = 1$)

eventually results in the minimization of Rayleigh quotient (compare⁴⁶)

$$\tilde{z}_t^* = \underset{\tilde{z}_t \mid \langle \tilde{z}_t, \rho_t \rangle = 0}{\operatorname{argmin}} \frac{\tilde{z}_t^\top L_t \tilde{z}_t}{\tilde{z}_t^\top D_{\rho_t} \tilde{z}_t}, \quad (13)$$

where D_{ρ_t} is a diagonal matrix with ρ_t as its diagonal entries and $\langle \cdot, \cdot \rangle$ is the standard scalar product.

The solution to this problem \tilde{z}_t^* is given by the eigenvector to the second smallest eigenvalue of L_t ^{36,46}. We choose its sign such that the virtual tile $A_{t,\nu}$ has a negative entry. Since the virtual tile is definitely not part of the inner set C_t , more positive values indicate membership with the inner coherent core. This eigenvector \tilde{z}_t^* may be thresholded at different values to generate an indicator vector \bar{z}_t and partitions of different size. In the next section, we present how to find the optimal threshold.

B. Coupling of Adjacent Time Steps

At the end of the first analysis step, we obtained a sequence of independent real-valued indicator vectors \tilde{z}_t^* for each time-step t that quantify the affiliation of each tile $A_{t,i}$ with the coherent core $S_t \subset X_t$. In the second step, we use thresholds for these indicator vectors \tilde{z}_t^* to partition the domains X_t in inner coherent core S_t and outer surrounding flow F_t . These thresholds are determined by coupling adjacent time-steps via short-time transfer operators $P_t'^\pm$ (see Fig. 2) and maximizing the overall probability c to stay within the inferred sequence of sets S_t .

For each individual time step t , we threshold the indicator vector \tilde{z}_t^* to obtain a thresholded indicator vector \bar{z}_t that determines the inner core S_t . It is furthermore practical to define a thresholded indicator vector \bar{z}_t by the mass m_t of the coherent core S_t it defines. Let $\Theta(\cdot)$ be the heavy-side function, then

$$\bar{z}_{t,i}(m_t) := \Theta(\tilde{z}_{t,i}^* - \vartheta_t(m_t))$$

$$\text{such that } \sum_i \bar{z}_{t,i} \rho_{t,i} \approx m_t \quad (14)$$

defines the inner core S_t with mass close to m_t via

$$S_t(m_t) := \bigcup_{i \mid \bar{z}_{t,i}=1} A_{t,i}. \quad (15)$$

Computationally, the correct threshold ϑ_t for every mass m_t can be found using a line search.

Thus, given a sequence of masses m_t , we generate thresholded indicator vectors $\bar{z}_t(m_t)$ that define a sequence of estimated coherent sets S_t with approximately these masses.

However, these partitionings should not be independent from each other since they all describe the evolution of the same coherent structure. So, in order to couple domains X_t , $X_{t\pm 1}$ that are adjacent in time, we compute short-time transfer operators $P_t'^\pm$ that quantify the transport from one domain X_t to the next $X_{t\pm 1}$ using Ulam's method (see Fig. 2a), one for each time direction.

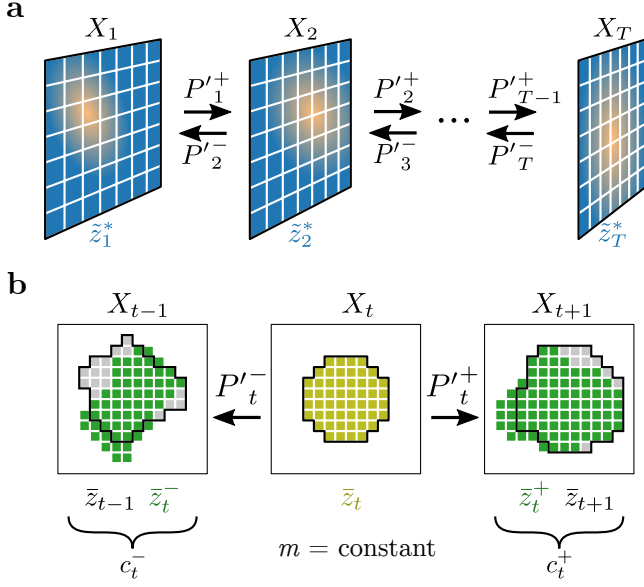


FIG. 2. **Generation of coherence ratios** **a)** The analysis step is used to compute indicator vectors \tilde{z}_t^* for each domain X_t individually. In addition, we compute transfer operators $P_t'^{\pm}$ that connect adjacent time-steps. **b)** We threshold each indicator vector such that the mass m of the inner set is the same for each thresholded indicator vector \tilde{z}_t . The vector \tilde{z}_t is transported via $P_t'^{\pm}$ and thresholded under the same premise to obtain \tilde{z}_t^{\pm} . Comparing the transported \tilde{z}_t^{\pm} with the thresholded indicator vectors of adjacent time-steps $\tilde{z}_{t\pm 1}$ yields the coherence ratios c_t^{\pm} .

From there, we compute normalized transfer operators Q_t^{\pm} by means of

$$\eta_t^{\pm} = \rho_t P_t'^{\pm} \text{ and} \quad (16)$$

$$Q_t^{\pm} = D_{\rho_t} P_t'^{\pm} D_{\eta_t^{\pm}}^{-1}. \quad (17)$$

Here, D_v is a diagonal matrix with v on its diagonal. These operators conserve the one-vector and can thus properly transport the indicator vectors \tilde{z}_t^* into the future and past

$$\tilde{z}_t^{*,\pm} = \tilde{z}_t^* Q_t^{\pm}. \quad (18)$$

These indicator vectors $\tilde{z}_t^{*,\pm}$ are again thresholded such that the resulting partitioning in the adjacent domains $X_{t\pm 1}$ have the mass m_t , i.e.

$$\tilde{z}_{t,i}^{\pm} = \Theta(\tilde{z}_{t,i}^{*,\pm} - v_t^{\pm}) \text{ such that } \sum_i \tilde{z}_{t,i}^{\pm} \eta_{i,t} \approx m. \quad (19)$$

This defines the a transported coherent core S_t^{\pm} in the adjoining domains by

$$S_t^{\pm}(m_t) = \bigcup_{i | \tilde{z}_{t,i}^{\pm}(m_t)=1} A_{t\pm 1,i}^{\pm}. \quad (20)$$

Now, the probability of starting in the set $S_t \subset X_t$ and being transported into the next set $S_{t\pm 1} \subset X_{t\pm 1}$ can be

expressed by

$$\begin{aligned} p(x_{t\pm 1} \in S_{t\pm 1} | x_t \in S_t) \\ = \frac{\mu(\Phi^{-1}(S_{t\pm 1}, t \pm 1, t) \cap S_t)}{\mu(S_t)} \\ \approx \frac{\tilde{z}_t^{\pm} D_{\eta_t^{\pm}} \tilde{z}_{t\pm 1}}{\tilde{z}_t^{\pm} D_{\eta_t^{\pm}} \tilde{z}_t^{\pm}} := c_t^{\pm}. \end{aligned} \quad (21)$$

This defines c_t^{\pm} , the next-time coherence ratios of transport into the future and past (see Fig. 2b). Averaging these coherence ratios geometrically yields

$$c^{\pm} = \sqrt[r-1]{\prod_t c_t^{\pm}}, \quad (22)$$

average coherence ratios that depict the probability to stay in the inferred inner cores S_t for one time step in each time direction. We define the average of these quantifies, the total averaged coherence ratio

$$c = \frac{1}{2} (c^+ + c^-), \quad (23)$$

to be the target function of our optimization.

Maximizing the total averaged coherence ratio is no simple task since it critically depends on all masses m_t . Different options are conceivable to facilitate the optimization process. For example, it would be possible to use a greedy or block-greedy combination of line searches starting from the end points $t = 1, T$. It would also be conceivable to fix a minimum value of either c_t^+ or c_t^- , to maximize the other and to follow the corresponding time direction. Both would lead to different results that focus on different aspects of coherent sets.

Under the condition that the underlying flow Φ is not too divergent, we here propose to simply set $m_t = m$ for all t with the idea that the Lebesgue mass of the coherent volume should not change significantly. This reduces the optimization of T masses to the question which mass m maximizes the total averaged coherence ratio c .

C. Evaluating Results

Two different measures are useful to investigate the validity during analysis: the sequence of second smallest eigenvalues λ_t used to compute the eigenvector \tilde{z}_t^* and the sequences of coherence ratios c_t^{\pm} .

The larger λ_t the less coherent the partitioning determined by thresholding \tilde{z}_t^* will be. Hence, we will find peaks in the eigenvector λ_t whenever the structures in the flow become less coherent.

The sequence of coherence ratios c_t^{\pm} for a given mass m_t but most likely for all masses will show a similar behavior. However, since the coherence ratios operate on the thresholded indicator vectors \tilde{z}_t , the impact of sudden changes in the velocity field will be more dramatic. Rapid changes in c_t^{\pm} also indicate moments in which the assumption that the mass of the coherent volume does not change is not fulfilled. In these moments filaments might be shed or entrained or the eddy might become

generally unstable and vanish in favor of another structure.

This means, that the investigation of the evolution of eigenvalues λ_t and the sequence of coherence ratios c_t^\pm gives insights into the development of the coherent water mass and helps to check the plausibility of the assumptions that form the basis of the following optimization.

More practically, it helps to find the intervals in which the existence of coherent volumes of constant mass is probable and helps to identify where the method is not able to find concrete results. We will see that this comes in handy if real oceanic data is investigated.

III. RESULTS

We test the presented approach by means of three different models. First, we investigate the qualifications of this approach using a stationary velocity field of Gaussian vortices (see³⁶). In the second test, we aim to find the coherent set in the wake of a Bickley-jet³⁸, a non-stationary flow and standard in the field³⁵. And finally, we apply our approach to real oceanic velocity fields of the Baltic Sea.

In all cases we follow the same scheme and use an linearly interpolated gridded velocity field in discrete time as starting point of our investigations since this is the data format of real oceanic velocity fields. Trajectories in this velocity field are generated by means of numerical integration using Heun's method.

A. Stationary Flow

First, we test our approach using a stationary two-dimensional velocity field. Since, in these flows, separatrices form the natural barriers between coherent sets of maximal size, we are able to investigate whether and to which extent our approach is able to recover the ground truth in a simple scenario.

For this check, we use a stationary Gaussian blob model. Velocity fields generated by this approach are given by

$$\mathbf{v}(\mathbf{x}) = -\frac{1}{2\pi} \sum_{i=1}^M \frac{\Gamma_i \left(1 - \exp\left[-\frac{(\mathbf{x}-\mathbf{x}_i)^2}{2\sigma_i^2}\right]\right)}{(\mathbf{x}-\mathbf{x}_i)^2} (\mathbf{x}-\mathbf{x}_i) \times \hat{\mathbf{e}}_z \quad (24)$$

where Γ_i and σ_i are vorticity and standard deviation of individual Gaussian vortices. Time and distances are measured in arbitrary units.

For our test, we choose the same parameters as in³⁶, i.e. three similar vortices with negative vorticity surrounding a vortex with positive vorticity. The aim is to recover the maximal central coherent set and thus the separatrices of the central eddy (see Fig. 3a).

We use this model to generate a gridded velocity field in the quadratic domain confined by the vertices $\mathbf{x} = (\pm 2, \pm 2)$ with a spatial resolution of $\delta x = 0.008$. Even though the model is stationary, we need a temporal resolution to treat the model as a real data set.

Therefore, we choose a time step of $h = 0.02$ between subsequent time steps and create a sequence of velocity fields of length $T = 200$.

Using this data set, we first compute the Okubo-Weiss criterion Q . On the basis of this field Q we choose the domain of interest X by hand (see Fig. 3a). Since the flow is stationary, we choose X to be the same for each time step.

For the numeric integration of the velocity field, we use the minimal time step of the data set $\delta t = 0.02$. The integration time to generate the transfer operator is set to $\tau = 0.9$ and couple subsequent time steps with $\tau' = h = 0.02$. Next-time coherence ratios are computed for $M = 500$ different masses.

Since the model and the sequence of domains is stationary and the mass is forced to be stationary too, the sequences of future and past next-time coherence ratios c_t^+, c_t^- are also stationary. The averaged future and past coherence ratios c_t^+, c_t^- first increases strongly with mass m and display a noisy plateau for intermediate masses m before decreasing rapidly (see Fig. 3b). This is the expected behavior for stationary flows that exhibit a foliated hierarchy of coherent structures: Each orbit around the central elliptic fixed point confines a coherent set. Since all coherent sets are in principle equivalent and differences in the coherence ratio are only caused by the placement and resolution of the tiled covering, the averaged coherences rarely exhibit a distinct maximum.

However, larger coherent masses should on average appear more coherent than smaller masses because of the tiling's finite resolution. Thus, in order to decide which mass to choose for the threshold, we smooth the total averaged coherence ratio c using a standard Savitzky-Golay filter of third order with a window size of 21 steps. The smoothed total average coherence ratio \tilde{c} shows a clear unimodal structure with a distinct maximum suitable for threshold selection (see Fig. 3b).

This threshold yields a partitioning that satisfactorily approximates the separatrices of the flow (see Fig. 3b). Test tracers released in the recovered eddy core do not leave the inner set (up to tiling resolution) for 249 integration steps, more than five times the observation horizon of the analysis of each individual time step.

B. Bickley Jet

Here, we study the results of our approach using a time-dependent Bickley jet flow³⁸. The model that describes an idealized stratospheric flow of two interacting Rossby waves is given by the stream function

$$\begin{aligned} \Psi(x, y, t) = & -U_0 L \tanh\left(\frac{y}{L}\right) \\ & + U_0 L \operatorname{sech}^2\left(\frac{y}{L}\right) A_2 \cos(k_2[x - c_2 t]) \\ & + U_0 L \operatorname{sech}^2\left(\frac{y}{L}\right) A_3 \cos(k_3[x - c_3 t]) . \end{aligned} \quad (25)$$

where $L = 1700$ km is the characteristic length scale and $U_0 = 62.66$ m/s is the characteristic velocity. $k_n = 2n/r_e$ are meridional wave numbers on a sphere with the radius of the earth $r_e = 6371$ km at 60° latitude. We adopt all

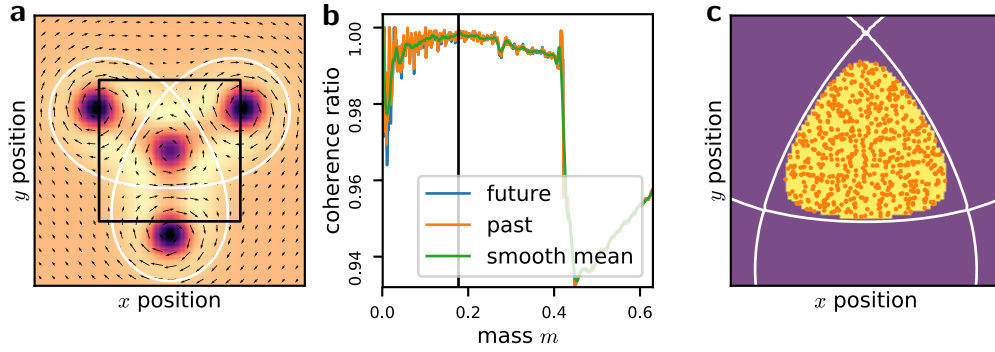


FIG. 3. **Stationary flow.** **a)** Velocity field of flow with Okubo-Weiss criterion in the background. White: Separatrices. Black: Domain choice. **b)** Average future c^+ (blue) and past c^- (orange) coherence ratios display a rather noisy signal. Smoothing the total mean coherence ratio c (green) results in a curve with a distinct maximum (black vertical line). **c)** The partitioning defined by the mass of this maximum results in a good approximation of the inner set (yellow) that fills the separatrices. Tracers (orange) do rarely cross the boundary and stay mostly inside the inferred inner region.

parameter values from³⁸, i.e. $c_2/U_0 = 0.205$, $c_3/U_0 = 0.461$ and $A_2 = 0.1$ and $A_3 = 0.3$. The velocity field is given by $\mathbf{v}(x, y, t) = (\partial_y \Psi(x, y, t), -\partial_x \Psi(x, y, t))$. This parameter set results in a quasiperiodic stream function that generates a meandering jet surrounded by a zone of Lagrangian chaos and several vortices that move with constant velocity.

For the data set, we choose a spatial and temporal resolution of $\delta x = 80$ km and $\delta t = \frac{1}{4}$ h as well as a duration of $T = 10$ days. We choose a small time step to reduce errors of non-symmetric numeric integration for an integration time of 6 days.

Using this data set we compute the Okubo-Weiss criterion and select an initial domain of interest X_1 (see Fig. 4a). Domains for other times X_t are selected by moving the initial domain X_1 with an appropriate constant velocity of $v_x = 105$ km/h along the x -axis. We set the integration time to $\tau = 2$ days and couple intervals of $\tau' = 1$ h. Each domain is partitioned into square tiles with a side length of $\Delta x = 80$ km.

Our approach generates future and past next-time coherence ratios c_t^+ , c_t^- over 6 days (see Fig. 4b for c_t^+ as a reference). While small sets apparently result in an inconsistent flickering of the coherence ratio sequence, large sets are consistently less coherent than sets of intermediate size. The averaged future and past coherence ratios c^+ and c^- display the same weakly noisy and unimodal dependence on the mass m that exhibits a distinct maximum for intermediate masses (see Fig. 4c). Using the maximum of the total averaged coherence ratio c as a threshold to determine the best partitioning results in reasonable structures (see Fig. 4d). The integration of test particles from the start of the analysis to the end of the analysis reveals that most particles stay inside the structure, i.e. in all inferred eddy cores (golden dots). And not all test particles that leave the structure at some point (blue, orange, green) do generate filaments; many remain in the vicinity of the uncovered eddy core.

Parts of the leakage might be explained by ghosting, i.e. trajectories in the vicinity of the actual eddy boundaries that diverge too slowly to be detected within the considered observation horizon of $\tau = 2$ days.

Apart from this small leakage at the corners, regions

that are difficult to resolve (see Fig. 3c for comparison), our method yields good results.

C. Baltic Sea

Finally, we apply our approach to a real data set of oceanic velocity fields.

The data set was generated by the coastal ocean model GETM (General Estuarine Transport Model)^{47,48} of the Western Baltic Sea. The setup of the model is chosen as in⁴⁹ and²⁵. The studied area has a horizontal spatial resolution of 1/3 nautical miles (approx. 600 m). 50 terrain-following adaptive layers focused towards stratification were used for the vertical resolution. In a post processing step the terrain-following coordinates were interpolated to an equidistant vertical spacing of 1 m and averaged over the upper 10 m of the water column to produce a quasi two-dimensional field. The velocity fields are part of a multidecadal simulation and cover the timespan March 2010 to October 2010. The temporal resolution of the velocity fields is 1 h. More details of the coupled setup of GETM can be found in^{25,39} where the data set was originally used.

We use a Lagrangian descriptor, the MV-tool²⁵, to identify all eddies with a lifetime longer than 100 h that travel more than 8 km (see³⁹ for details). From this eddy data set, we select eight test eddies by hand for detailed analysis. Since the discussion of all eight eddies exceeds the scope of the article, we focus on the analysis of eddy E1 and E2: Eddy E2 serves as an example of mostly effortless reconstruction while eddy E1 illustrates how the investigation of the future and past next-time coherence ratio sequences help to find intervals of plausible coherence and improve our results.

In all cases the sequence of domains of interest X_t is generated automatically on the basis of the eddy polygon returned by MV because the sheer amount of data renders manual selection impractical (circa 250 time steps per eddy). For this purpose, we first analyze the distribution of polygon area provided by the proxy and select an appropriate area value for all domains of interest. Under the assumption that the mass of the coherent eddy

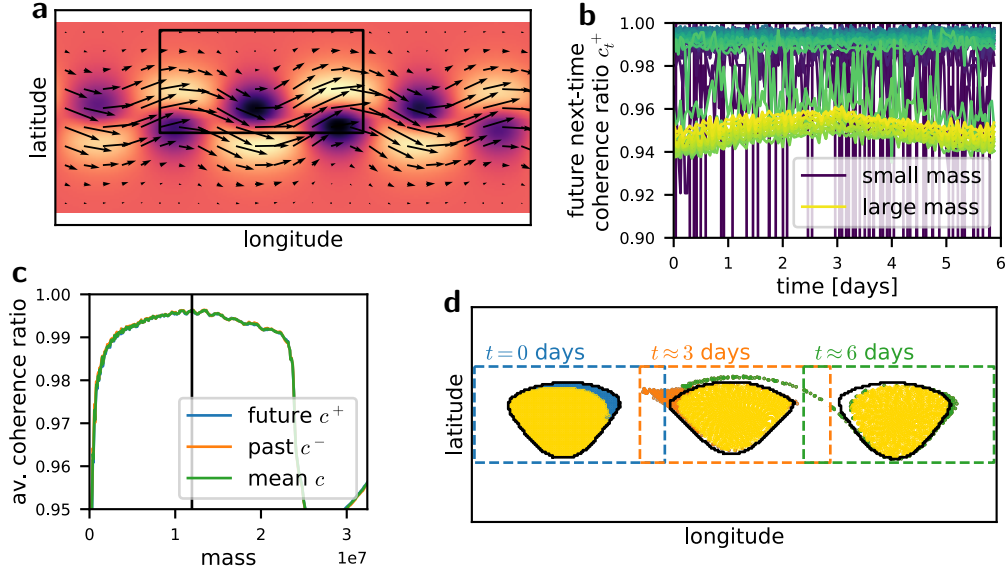


FIG. 4. **Analysis results for the Bickley jet.** (a) Velocity field of the model with Okubo-Weiss field Q in the background. A minimum of Q is tracked and surrounded by a domain of interest X (black). (b) Future next-time coherence ratio c_t^+ for the complete analysis of 6 days for 50 of 500 masses. Small masses (blue) result in inconsistent flickering and large masses (yellow) are less coherent than intermediate masses (light blue, green). (c) Average future and past coherent ratios c^+ , c^- and total averaged coherence ratio c dependent on the mass m . The figure shows a distinct maximum. (d) Returned boundary estimates of the coherent volume (black) and considered domain of interest X at three different times (blue, orange, green dashes). Comparison of integrated particles that are contained in the structure at all times (gold) and those that leave the structure at least once at different time (blue, orange, green dots). Only a few particles leave the structure and form filaments.

core does not change, the domain of interest should be larger than the size of the eddy core. However, choosing an area value that is too large might incorporate additional coherent volumes like slowly mixing filaments and other eddy cores that interfere with the analysis. Hence, an appropriate area value is much larger than the average polygon area but smaller than any unreasonable outlier. Next, we find the centroid of each polygon and its longitudinal and latitudinal proportions. The domain of interest in each time step is then chosen to be a rectangle with the determined centroid, area and proportions. This method of automatic domain selection compensates occasional rapid changes of MV. However, also non-rectangular, automated domain selection methods are conceivable. In any case, minor changes in the geometry or the placement of the domain should have no significant impact on the analysis.

Furthermore, we set the integration time for the transfer operator P to $\tau = 36$ h and couple adjacent time steps, i.e. $\tau'_{E2} = 1$ h and $\tau'_{E1} = \{1, 2\}$ h since some data was missing. In order to enhance symmetry of numerical integration, we set the integration time step to $\delta t = 1/4$ h and interpolate linearly in time and space.

Eddy E2 starts from an upwelling zone at the coast of Rügen at April 5th, 2010 and travels north-east (see Fig. 5a).

Investigating the evolution of future and past next-time coherence ratios c_t^+ , c_t^- reveals some but no significant structure: no drastic changes in the coherence ratio are visible and intermediate masses yield the best results (see Fig. 5b).

Averaging over time for each mass m results in the averaged coherence ratio curves c^+ , c^- (see Fig. 5c).

Smoothing the total averaged coherence ratio c by means of an Savitzky-Golay filter (window size 51, order 3) results in a distinct maximum that can be used for thresholding. Interestingly, the averaged future coherence ratio c^+ is persistently larger than the averaged past coherence ratio c^- . Since integration of particles is mostly time-symmetric within the observation horizon, this is a strong indicator for a non-divergence free velocity field with a sink: Mass is contracted and collected in the center of the structure and thus reducing the probability to be transported across the boundary while the opposite effect occurs in backwards time-direction.

Observing the trajectories of test tracers injected in the first inferred boundary reveals that most tracers stay within *all* following boundaries. And even those particles which leave the structure at least once stay in the vicinity; only few form filaments (see Fig. 5). Moreover, the particles contract slightly what confirms a non-divergent free velocity field presumably generated by downwelling.

Eddy E1 starts at the northern coast of Rügen at March 6th, 2010 where it stays almost all its lifetime (see Fig. 6a).

Taking a look at the next-time coherence ratios reveals sudden drops and rapid changes (see Fig. 6b). We conclude that the presented method is not able to find a structure that is coherent over the complete given time interval. This might be caused by two factors: First, the assumptions necessary for the application of the presented method are not fulfilled or, secondly, no eddy core with stable mass exists over the full time interval. The former occurs if the mass of the eddy core changes quickly (assumption of constant mass) or domains where not chosen correctly (assumption of domain consistency). The

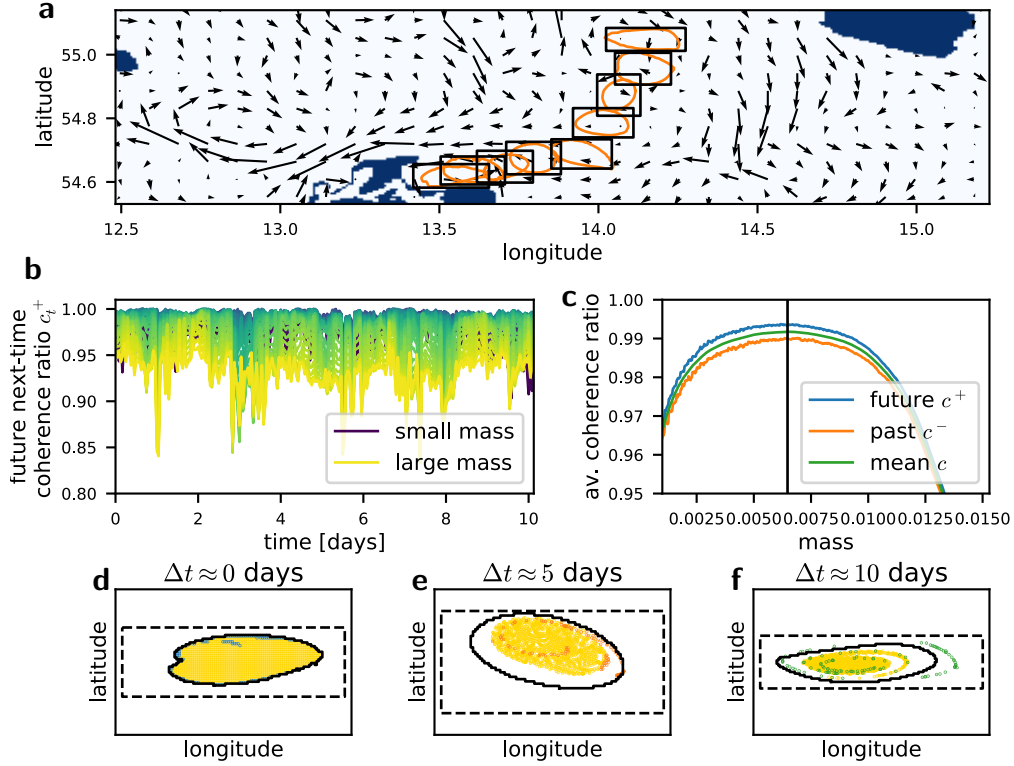


FIG. 5. **Eddy E2** (a) Overview of eddy path and associated domains of interest. Every 10th polygon is shown. Velocity field for $t = 0$, i.e. 11:00 am, April 5th, 2010. (b) The sequence of future next-time coherence ratios c_t^+ shows some structure but no rapid changes. Again intermediate masses show best results. Past next-time coherence ratios c_t^- show a similar behavior. (c) Averaged future and past coherence ratio c^+ , c^- and smoothed total mean coherence ratio c depending on mass m show distinct maximum used for thresholding (black). Persistent $c^+ > c^-$ is an indicator for downwelling. (d/e/f) Eddy boundary (black) and particle positions injected at the beginning (a), middle (e) and end (f) of the structures life show that most particles remain within all detected boundaries (yellow). Particles that leave the boundaries at least once mostly stay within the boundaries and produce only minor filaments (blue/orange/green). Contraction of particle cloud reveals downwelling.

latter occurs, if the eddy is deformed too much to justify coherence, e.g., when it collides with a front. The structures detected by MV may lose their coherence by shedding filaments. If a smaller coherent eddy core remains, old and new core might still be detected as one consistent structure by MV.

MV is after all only a proxy that investigates time steps individually. In any case, the analysis of next-time coherence ratios lets us identify time intervals that are suited for the presented approach. We simply choose a window of persistently high coherence to select a plausible analysis window for the presented method.

Investigating the coherence ratios averaged over this time interval c^+ , c^- , c (c again smoothed using a filter Savitzky-Golay filter of third order with a window size of 21 steps) reveals a maximum that can be used to define the threshold (see Fig. 6c). We again observe consistently larger future next-time coherence ratios than past next-time coherence ratios indicating a slight contraction of mass.

Investigating the trajectories of particles injected in the boundaries at the beginning of the analysis interval, we find the same effects we already found when evaluating the results of eddy E2: Most particles stay in *all* inferred boundaries, no large filaments are generated and

mass contraction is confirmed.

IV. CONCLUSION

In this article, we presented a modified extended two-step transfer operator approach following ideas of^{31,36,37}.

The first analysis step generates indicator vectors that provide a ranking of domain parts for individual points in time. Modifications of the transfer operator deal with coastline fluxes, help to focus on larger water bodies and ensure that the domain is partitioned in an inner and an outer set. While the computation of indicator vectors follows ideas of classical transfer operator methods³¹ all modifications to the transfer probability matrix are novelties in the style of³⁶ that increase overall performance.

In the second analysis step, we search for appropriate indicator vector thresholds that result in one consistent and maximally coherent structure over time. We assume a divergent free velocity field and relax the optimization procedure to a line search. During this step an appropriate time-interval may be chosen to guarantee that critical assumptions hold. Aside from general assumptions like persistent coherence and correct domain selection that can be checked using the next-time coherence ratios, it

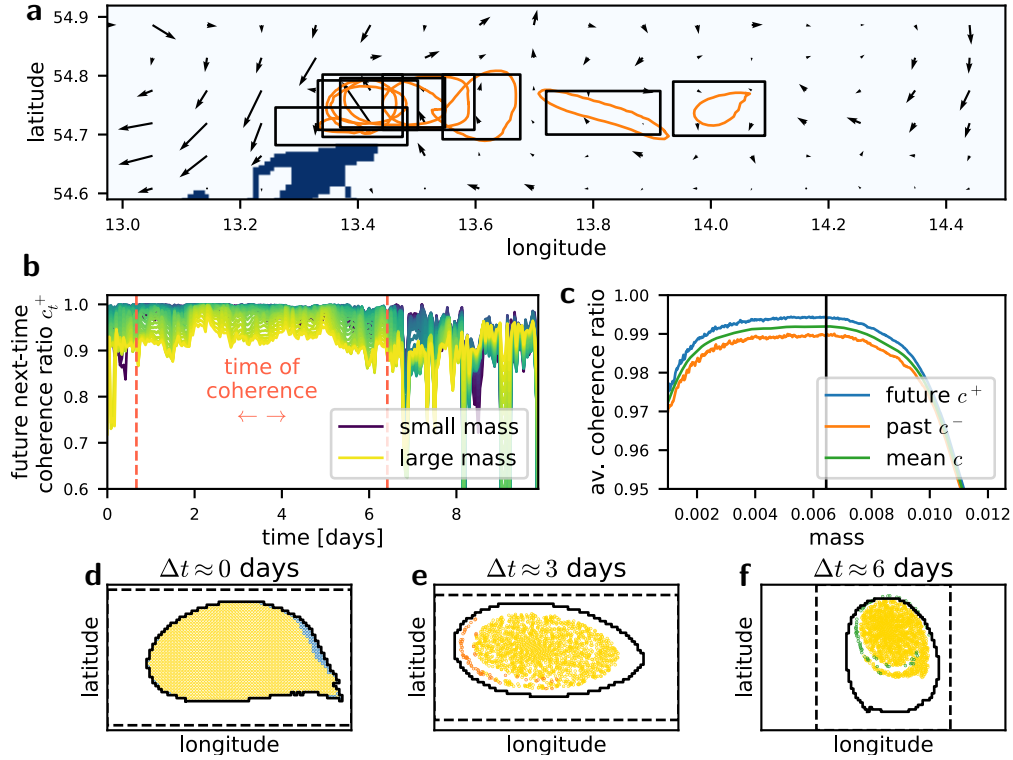


FIG. 6. **Eddy E1** (a) Overview of eddy path and associated domains of interest. Every 10th polygon is shown. Velocity field for $t = 0$, i.e. 19:00 am, March 6th, 2010. (b) The sequence of future next-time coherence ratios c_t^+ shows rapid changes between which no real coherence exists. A window without rapid changes is identified for further analysis. (c) Averaged future and past coherence ratio c^+ , c^- and smoothed total mean coherence ratio c depending on mass m display maximum for intermediate masses (black). Persistent $c^+ > c^-$ is an indicator for downwelling. (d/e/f) Again, eddy boundary (black) and particle positions injected at the beginning, at the beginning (a), middle (e) and end (f) of the structure's life show that most particles remain within all detected boundaries (yellow). Particles that leave the boundaries at least once mostly stay within the boundaries and produce no minor filaments (blue/orange/green). Contraction of particle cloud reveals downwelling.

is also possible to check whether the velocity field is divergent free, by looking at the averaged coherence ratios. This analysis step constitutes a major change to former methods which mainly focused on the treatment of isolated points in time.

We tested our approach using a stationary and a quasi-periodic model as well as actual oceanic velocity field data. In the stationary case, we were able to approximate the separatrices well (see Fig. 3). The uncovered structures stayed coherent for times much longer than the observation horizon. In the quasi-stationary case, a Bickley jet model, our approach resulted in a sequence of boundaries that displayed high coherence.

Likewise, the study of real oceanic velocity fields yielded good results. We analyzed eight Baltic eddies in total. The results are used in a study of plankton population dynamics in coherent eddy cores³⁹ to guarantee a common history of water parcels.

Here, two eddies have been discussed in detail. The results of both eddies displayed high coherence; most particles stayed in all inferred boundaries in forwards time direction (see Fig. 5 and Fig. 6). Moreover, the application of our method to eddy E1 showed that the approach is able to find plausible time windows for valid application (see Fig. 6b). In both cases we noticed and confirmed that the velocity field was not divergent free. We found

that mass was slightly contracting within the inferred boundaries and thus that the assumption of volume conservation was not perfectly fulfilled. Hence, particles injected into the last boundary and integrated backwards in time leave the inferred structures with a significantly higher probability.

In summary, testing the presented approach was a success. Our method found sequences of boundaries with high coherence in all scenarios. In addition, our method is able to find appropriate time intervals for its application which renders its results more trustworthy. For future applications, further improvements are conceivable: It is straight forward to improve the domain selection procedure by allowing non-rectangular domain choices. Instead of only coupling adjacent time steps, a weighted average over a range of different time differences might also improve the approach. And most importantly, the usage of a more sophisticated optimization routines would allow the treatment of divergent velocity fields.

In conclusion, we were able to show that modified transfer operator methods and approaches that take temporal development of structures into account have high potential of uncovering the boundaries of eddy cores.

Acknowledgments. We would like to thank Ulrike Feudel, Maximilian Berthold and Ulf Gräwe for valuable discussions and helpful feed-back.

Moreover, we are grateful to Ulf Gräwe (Leibniz Institut für Baltic Sea Research, Warnemünde) for providing the velocity field data set of the Baltic Sea and to the "Norddeutsche Verbund für Hoch- und Höchstleistungsrechnen (HLRN)" for access to their high-performance computing center. The analyzed model data was generated on the HLRN.

Most parts of the eddy tracking based on MV were performed at the HPC Cluster CARL, located at the University of Oldenburg (Germany) and funded by the DFG through its Major Research Instrumentation Programme (INST 184/157-1 FUGG) and the Ministry of Science and Culture (MWK) of the Lower Saxony State.

Rahel Vortmeyer-Kley would like to thank BMBF-HyMeSimm FKZ 03F0747C for funding.

- ¹J. Aristegui, P. Tett, A. Hernández-Guerra, G. Basterretxea, M. F. Montero, K. Wild, P. Sangrá, S. Hernández-León, M. Cantón, J. A. García-Braun, M. Pacheco, and E. D. Barton, Deep-Sea Research Part I: Oceanographic Research Papers **44**, 71 (1997).
- ²A. Martin, Progress in Oceanography **57**, 125 (2003).
- ³L. M. Beal, W. P. M. De Ruijter, A. Biastoch, R. Zahn, M. Cronin, J. Hermes, J. Lutjeharms, G. Quartly, T. Tozuka, S. Baker-Yeboah, T. Bornman, P. Cipollini, H. Dijkstra, I. Hall, W. Park, F. Peeters, P. Penven, H. Ridderinkhof, and J. Zinke, Nature **472**, 429 (2011).
- ⁴C. Dong, J. C. McWilliams, Y. Liu, and D. Chen, Nature Communications **5**, 1 (2014).
- ⁵J. Karstensen, B. Fiedler, F. Schütte, P. Brandt, A. Körtzinger, G. Fischer, R. Zantopp, J. Hahn, M. Visbeck, and D. Wallace, Biogeosciences **12**, 2597 (2015).
- ⁶M. Sandulescu, C. López, E. Hernández-García, and U. Feudel, Nonlinear Processes in Geophysics **14**, 443 (2007).
- ⁷F. D'Ovidio, S. De Monte, S. Alvain, Y. Dandonneau, and M. Levy, Proceedings of the National Academy of Sciences **107**, 18366 (2010).
- ⁸S. Prants, M. Budyansky, and M. Y. Uleysky, Deep Sea Research Part I: Oceanographic Research Papers **90**, 27 (2014).
- ⁹D. J. McGillicuddy, Annual Review of Marine Science **8**, 125 (2016).
- ¹⁰A. Bracco, A. Provenzale, and I. Scheuring, Proceedings of the Royal Society B: Biological Sciences **267**, 1795 (2000).
- ¹¹P. Gaube, D. J. McGillicuddy, D. B. Chelton, M. J. Behrenfeld, and P. G. Strutton, Journal of Geophysical Research: Oceans **119**, 8195 (2014).
- ¹²L. Brannigan, Geophysical Research Letters **43**, 3360 (2016).
- ¹³A. P. Martin, K. J. Richards, A. Bracco, and A. Provenzale, Global Biogeochemical Cycles **16** (2002), 10.1029/2001GB001449.
- ¹⁴A. Okubo, Deep-Sea Research and Oceanographic Abstracts **18**, 789 (1971).
- ¹⁵J. Weiss, Physica D: Nonlinear Phenomena **48**, 273 (1991).
- ¹⁶J. Isern-Fontanet, E. García-Ladona, and J. Font, Journal of Atmospheric and Oceanic Technology **20**, 772 (2003).
- ¹⁷A. Chaigneau, A. Gizolme, and C. Grados, Progress in Oceanography **79**, 106 (2008).
- ¹⁸S. Itoh and I. Yasuda, Journal of Physical Oceanography **40**, 1018 (2010).
- ¹⁹D. B. Chelton, M. G. Schlax, and R. M. Samelson, Progress in Oceanography **91**, 167 (2011).
- ²⁰F. Nencio, C. Dong, T. Dickey, L. Washburn, and J. C. McWilliams, Journal of Atmospheric and Oceanic Technology **27**, 564 (2010).
- ²¹J. C. McWilliams, Journal of Fluid Mechanics **219**, 387 (1990).
- ²²G. Boffetta, G. Lacorata, G. Redaelli, and A. Vulpiani, Physica D: Nonlinear Phenomena **159**, 58 (2001).
- ²³S. C. Shadden, F. Lekien, and J. E. Marsden, Physica D: Nonlinear Phenomena **212**, 271 (2005).
- ²⁴A. M. Mancho, S. Wiggins, J. Curbelo, and C. Mendoza, Communications in Nonlinear Science and Numerical Simulation **18**, 3530 (2013).
- ²⁵R. Vortmeyer-Kley, U. Gräwe, and U. Feudel, Nonlinear Processes in Geophysics **23**, 159 (2016).
- ²⁶A. Hadjighasem, D. Karrasch, H. Teramoto, and G. Haller, Physical Review E **93**, 1 (2016), 1506.02258.
- ²⁷G. Froyland and K. Padberg-Gehle, Chaos: An Interdisciplinary Journal of Nonlinear Science **25**, 087406 (2015).
- ²⁸G. Haller and F. J. Beron-Vera, Journal of Fluid Mechanics **731**, R4 (2013), 1308.2352.
- ²⁹M. Farazmand, D. Blazevski, and G. Haller, Physica D: Nonlinear Phenomena **278-279**, 44 (2014).
- ³⁰G. Haller, Annual Review of Fluid Mechanics **47**, 137 (2015), 1407.4072.
- ³¹G. Froyland and K. Padberg-Gehle, Physica D: Nonlinear Phenomena **238**, 1507 (2009).
- ³²G. Froyland, N. Santitissadeekorn, and A. Monahan, Chaos: An Interdisciplinary Journal of Nonlinear Science **20**, 043116 (2010), 1008.1613.
- ³³G. Froyland, Physica D: Nonlinear Phenomena **250**, 1 (2013).
- ³⁴T. Ma and E. M. Bollt, International Journal of Bifurcation and Chaos **23**, 1330026 (2013).
- ³⁵A. Hadjighasem, M. Farazmand, D. Blazevski, G. Froyland, and G. Haller, Chaos: An Interdisciplinary Journal of Nonlinear Science **27**, 053104 (2017).
- ³⁶B. Lünsmann and H. Kantz, Chaos: An Interdisciplinary Journal of Nonlinear Science **28**, 053101 (2018).
- ³⁷G. Froyland, C. Horenkamp, V. Rossi, and E. van Sebille, Chaos: An Interdisciplinary Journal of Nonlinear Science **25**, 083119 (2015).
- ³⁸I. I. Rypina, M. G. Brown, F. J. Beron-Vera, H. Koçak, M. J. Olascoaga, and I. A. Udovychenko, Journal of the Atmospheric Sciences **64**, 3595 (2007).
- ³⁹R. Vortmeyer-Kley, B. Lünsmann, M. Berthold, U. Gräwe, and U. Feudel, Frontiers in Marine Science – Physical Oceanography, submitted (2018).
- ⁴⁰S. M. Ulam, (1964).
- ⁴¹G. Froyland, Physica D: Nonlinear Phenomena **200**, 205 (2005).
- ⁴²G. Froyland, K. Padberg, M. H. England, and A. M. Treguier, Physical Review Letters **98** (2007), 10.1103/PhysRevLett.98.224503.
- ⁴³M. Speetjens, M. Lauret, H. Nijmeijer, and P. Anderson, Physica D: Nonlinear Phenomena **250**, 20 (2013).
- ⁴⁴A. Denner, O. Junge, and D. Matthes, (2015), arXiv:1512.03761.
- ⁴⁵R. Banisch and P. Koltai, Chaos **27**, 1 (2017).
- ⁴⁶M. Dellnitz and O. Junge, SIAM Journal on Numerical Analysis **36**, 491 (1999).
- ⁴⁷K. Klingbeil and H. Burchard, Ocean Modelling **65**, 64 (2013).
- ⁴⁸K. Klingbeil, F. Lemarié, L. Debreu, and H. Burchard, Ocean Modelling **125**, 80 (2018).
- ⁴⁹U. Gräwe, M. Naumann, V. Mohrholz, and H. Burchard, Journal of Geophysical Research: Oceans **120**, 7676 (2015).